**Structure from motion used to revive archived aerial photographs for geomorphological analysis: An example from mount meager volcano, british columbia, canada**



*Published version:*

DOI:10.1139/cjes-2020-0140

# Structure for motion used to retrieve aerial photographs for geomorphological analysis  an example from Mount Meager volcano, British Columbia, Canada

Gioachino Roberti[1,2] , Brent C. Ward[2], Benjamin van Wyk de Vries[1], Luigi Perotti[3] , Marco Giardino[3] , Pierre A. Friele[4], John J. Clague[2], Brian Menounos[5], Leif S. Anderson[6], and Stefano Freschi[3].

(1) Université Clermont Auvergne, CNRS, IRD, OPGC, Laboratoire Magmas et Volcans, Aubiere Cedex, France (2) Earth Sciences Department, Simon Fraser University, Burnaby, British Columbia Canada(3) Earth Sciences Department, University of Torino, Torino, Italy(4) Cordilleran Geoscience, Squamish, British Columbia, Canada (5) Geography Program and Natural Resources and Environmental Studies Institute - University of Northern British Columbia, British Columbia, Canada. (6) GFZ German Research Centre for Geosciences, Postdam, Germany.

## Abstract

Topographic modeling has become more accessible due to the development of Structure from Motion (SfM) image matching algorithms in digital photogrammetry. However, little work has been done in using SfM with digitized historical airphotos. Large databases of historical airphotos are available in university, public, and government libraries, commonly as paper copies. The photos can be in poor condition (i.e. deformed by humidity, scratched, or annotated). In addition, the negatives, as well as metadata, may be missing. Processing such photos using classic stereo-photogrammetry is difficult and in many instances impossible. However, SfM can be applied to these photosets to access the valuable archive of geomorphic changes over the last century. In this study we digitized over 500 vertical airphotos, spanning from 1947 to 2006, of the Mount Meager volcano in southwest British Columbia, Canada. We use this data set to documented glacier and landslide activity at Mount Meager. Glaciers are generally retreating, with some local advances in 1960s and 1970s as documented at other glaciers in British Columbia. Landslide are common and contribute to the debris cover of the glaciers. The SfM processing of history airphotos allowed for a comprehensive, diachronic glacier change and landslide activity documentation, unlocking geomorphic information otherwise inaccessible. This approach could be more broadly applied, both in scientific and professional practices, to increase geomorphic knowledge over the past century improving future land planning and hazard management.

Keywords:, historical airphotos, Structure from Motion, glacier change, rock avalanche, debris covered glacier

## Introduction

Geomorphic reconstructions over time are fundamental in many landform and natural hazard studies. In support of these studies, aerial stereo-photogrammetry is classically used to produce topographic models and large-scale topographic maps, and has been made possible by acquisitions of a very large number of vertical aerial photographs around the world. The photos record Earth surface features that have changed over time or have completely disappeared, and they cover remote and difficult-to-access areas (e. g. high mountains and glacierized terrain) where establishing ground control is difficult or impossible (Chandler, 1999; Lane et al., 2000; Gomez, 2014; Gomez et al., 2015; Micheletti et al., 2015). Although historic airphotos are a unique and valuable resource for documenting surface changes over the $20^{th}$ century (Bjørk et al., 2012; Tennant and Menounos, 2013; Gomez et al., 2015), they are not extensively used for this purpose and commonly lie forgotten in university, government, public, and private libraries. Paper copies of old airphotos are commonly deformed by moisture, scratches, or annotations, and the original negatives or metadata on cameras and flight missions may be missing.

In these cases, it is difficult to retrieve topographic information from aerial photographs using classical digital photogrammetric techniques, although there are exceptions (e.g. Krimmel, 1999; Lucchesi et al., 2013; Tennant and Menounos, 2013). The Structure from Motion (SfM) method, on the other hand, can provide quantitative topographic and geomorphic information from these important data archives (Gomez, 2014; Gomez et al., 2015; Bakker and Lane, 2016; Mertes et al., 2017; Mölg and Bolch, 2017; Roberti et al., 2018b).

In this paper we use SfM and Lidar to document geomorphic change over a 69-year period (1947-2006 SfM; 2016 Lidar) at Mount Meager, a glacier-clad volcanic complex in southwest British Columbia, Canada (Figure 1). Our objective is to provide an example of the utility of SfM for analyzing geomorphic change from historical airphotos, by documenting six decades of glacier and landslide activity in five catchments draining the Mount Meager volcanic complex. Detailed galcier and landslide volume analysis for the whole Mount Meager is beyond the scope of this paper.

**Commentato [gr1]:** Focused the objective on SfM and geomorphic observation. leaving out most all the debris covered and volcano ice interaction consideration (for future publication)

### SfM origins and modern applications

**Commentato [gr2]:** I added this section. It should help the reviewers to better understand the approach we are proposing

The origin of SfM dates back to the seventies with the formulation of ―the Structure from Motion‖ theorem. SfM is the computer vision algorithm used to generate three-dimensional point clouds (Structure) in generic object coordinates from photographs taken by a moving sensor (Motion) (Ullman, 1979). In the geosciences, the term SfM refers to a composite workflow SfM-multi-view stereo (MVS) algorithm (Carrivick et al., 2016). At first instance, the SfM-MVS algorithm generates a sparse point cloud (SfM method) then creates a dense point cloud by increasing the number of points by the MVS method. In this chapter we will refer to the technique simply as SfM, in the general Geoscience connotation c.

Modern SfM was developed in the 1990's because of the increased availability of digital imagery. It entered the geosciences community in the past decade, after the studies of Cecchi et al., 2003, 2002) applied to laboratory models and aerial images taken from a hand held camera, and (Snavely et al., 2008) that reconstructed cities from photos randomly acquired by tourists. Today, SfM has diffused in all fields of Earth sciences, from the hand-sample scale reconstruction to medium-scale topographic modeling (James and Robson, 2012). This technique is commonly applied with pictures taken from a hand-held camera or unmanned aircraft vehicles (UAV) (Carrivick et al., 2016), and few studies have explored the possibility of processing archival airphotos from the past century for diachronic geomorphic studies (Gomez 2014; Gomez et al. 2015).

In the SfM workflow, the hardware can be a consumer-grade digital camera with the reconstruction coming from the redundancy of the images taken. SfM algorithms have been developed to work with off-nadir, convergent photos (Furukawa and Ponce, 2010; Snavely et al., 2008). SfM allows the three-dimensional reconstruction of objects and surfaces with sets of overlapping images, without the need of pre- calibrated metric cameras, ground control or any external information (Cecchi et al., 2003, 2002). The collinearity equations are solved using to the redundancy of images (Szeliski, 2010), without the need for ground control; hence the three-dimensional model is built a priori in generic x, y, z object coordinates. SfM photo matching is based on multiple scale image matching algorithms (e.g. the scale invariant feature transform, SIFT, Lowe, 1999) and global matching methods, where every pixel is matched (Hirschmüller et al., 2012). These algorithms recognize pixel gradients (e.g. shapes) to identify large numbers of common features between images. The ability to recognize shapes allows the matching of photos at different scales, translations, rotations and partially different brightness levels; it also allows the separation of objects from the background (Fonstad et al., 2013). The camera parameters are derived from self-calibration during the bundle adjustment. The SfM derived 3D point data quality depends only on the scale and quality of the pictures. The use of precise GCPs can also improve the bundle adjustment (Carrivick et al., 2016) and allows to produce georeferenced models, orthophotos and DEMs. In the case of lack of GCP, it is still possible to produce Orthophotos and DEMs and models can be scaled by defining the distance between recognizable points.

## Methods

We digitized 568 historic vertical aerial photographs and used the commercial SfM software PhotoScan to produce orthophotos and digital surface models (DSMs) from the digitized photos. PhotoScan delivered high-resolution orthophotos (0.42-1.13 m/pixel) and DSMs (1-5 m/pixel), suitable for our geomorphic study (Table 1). We processed part of the same dataset as Roberti et al. (2018b), using vertical black-and-white aerial photographs of Mount Meager taken in 1947, 1951,1962, 1964-1965, 1973, 1981, and 1990, and color photos taken in 2006. We also used an aerial Lidar digital terrain model (DTM) constructed from data acquired in 2015 and 2016. For this study, we processed images from 1947, 1962, 1964-1965, 1973, 1990, and 2006. A 1948 set of photos does not cover the entire volcanic complex and thus was excluded. The 1947 dataset covers the entire massif, but clouds partly obscure the land surface. The 1962 photos overlap poorly in the center of the massif, and snow covers most of the slopes. Lidar was used to assess the SfM-derived orthophoto quality and to extend the period of geomorphic analysis to 2016.

### Photo scanning

We used an A3 format flatbed scanner to digitize the airphotos. Each photo was scanned with the flight direction parallel to the charges-coupled device (CCD) array, following the recommendation of Linder (2009). The minimum DPIs (dots per inch) required for the scans were derived from the scale factor (S) of the photographs (Table 1), The photos and their metadata are listed in Table 1.

### PhotoScan processing

We used Agisoft PhotoScan Professional v1.2.6 SfM software (www.agisoft.com - Agisoft LLC, St. Petersburg, Russia) to process the digitized historical airphotos. We chose PhotoScan because it is widely use in the geosciences, has been proven to be reliable (Remondino et al., 2014; James et al., 2017), and includes a complete workflow from image matching to three-dimensional dense reconstruction, georeferencing, and orthophoto and DSM generation. We followed the standard PhotoScan workflow to generate orthophotos and DSMs, with particular attention to masking, referencing steps and optimization steps. We masked photo frames and inscriptions to speed up the processing and to prevent artifacts appearing in 3D models, orthophotos, and DSMs. We defined 22 ground control points (GCPs) on the standard base maps to reference 3D models. Planimetric coordinates were derived from satellite SPOT 10 m imagery, and vertical coordinates from the Canada TRIM (Terrain Resource Inventory Map) DEM (18.3 m average accuracy) (Natural Resources Canada, 2013). We used the Lidar DTM only for cartographic validation and not for georeferencing because we wanted to use a workflow that does not require Lidar and in which measurements can be done in relative coordinate systems. We selected ground control points in meadows, on glacier polished bedrock, on Little Ice Age moraines, along logging roads, and on other recognizable features. Not all the points are visible in all the datasets. In old aerial photos, for example, logging roads are not present and many higher elevation points are covered by snow.

Artifacts or voids are commonly generated in areas of lacking texture, for example glaciers, snowfields, forested areas, and shadows. Clouds can also obscure parts of the landscape, generating errors in the 3D models. Careful manual visual model examination was required to identify and delete artifacts. Table 1 summarizes the model characteristics for the different photo datasets, and further details on the processing are in Appendix A.

## Cartographic validation

The cartographic suitability of the PhotoScan generated orthophoto and DEMs was tested by comparison with a Lidar DEM acquired in 2015-2016. We followed two different approaches to assess the SfM products (Figure 2). First, we compared X, Y, and Z coordinates of 22 control points between the PhotoScan models and the Lidar reference. Secondly, we did raster to raster differencing between the datasets and the Lidar to evaluate the DEM quality. Then, to reduce systematic errors (tilting, doming etc.), we 1) re-aligned a subset of the photos and 2) co-registered DEM subsets in CloudCompare (Girardeau-Montaut, 2018). Photo re-alignment and DEM co-registration improved the DEMs, allowing more precise DEM comparison and volume calculations.

We tested the cartographic accuracy of the PhotoScan-generated orthophotos and DSMs by comparing them with the Lidar DTM acquired in 2015-2016. We compared X, Y, and Z coordinates of 22 control points (CP), which are not the same used in the Photoscan workflow, between the PhotoScan models and the Lidar DTM. Following ASPRS (2014) guidelines, we used the root mean square error (RMSE) to evaluate the accuracy of the SfM-derived cartographic products. We calculated the RMSE of x, y, z coordinates of at least 20 of the 22 control points (CP) (not all points are visible in all photos) taken from the PhotoScan exports and the reference Lidar DTM. $RMSE_x$, $RMSE_y$, $RMSE_z$, and $RMSE_r$ (horizontal linear RMSE, which includes both x- and y-coordinate errors). The horizontal accuracy at the 95% confidence limit (HA 95%) and the vertical accuracy at the 95% confidence limit (VA 95%) (ASPRS 2014). HA 95 and VA 95 approximate the maximum error on either side of the mean of 95% of the planimetric and altimetric values. Table 2 summarizes the $RMSE_x$, $RMSE_y$, $RMSE_z$, $RMSE_r$, HA 95, and VA 95 for the Lidar and photo check points. Horizontal georeferencing errors for these points range from 19 to 86 m; the corresponding vertical errors range from 15 to 176 m.

### DEM of difference

In order to better assess the error on the Z value of the SfM derived DEMs, we calculated the DEM of difference (DoD) between each dataset and the Lidar DEM. The SfM derived DEMs have systematic errors. The models are tilted, show doming effect or had steps between the different flight stripes. In order to reduce these errors we re- aligned subsets of photos and increased the number of control points in the PhotoScan processing. A smaller number of images requires less computational power, produces smaller, more manageable point clouds where wrongly projected points are easier to identify and remove. Also more control points can be easily placed; thus improving the overall 3D model generation and georeferencing process. Then we co- registered point cloud subsets in CloudCompare. The registration in CloudCompare eliminated the systematic tilting and corrected some of the doming effects, reducing errors to 1-10 m. Examples of DEM analysis 1990-2006 comparison of the pre-2010 collapse slope showing 1998 landslide scar (Bovis and Jakob, 2000) is in (figure 3A) and the 1975 landslide scar (Mokievsky-Zubok, 1977) at Devastation Valley (Figure 3B). In the pre-2010 collapse slope, it is possible to observe the glacier mass loss, a precursory failure from the toe of the slope, and an increase in displacement along the major fault that conditioned the failure (see Roberti et al., 2017) for more details about the 2010 failure.

**Commentato [gr3]:** Added DEM consideration

### GIS mapping

We describe the geomorphological evolution of the five main catchments on the Mount Meager massif (Figures2-6) based on the following. Glacier length is defined as the map distance from the highest point on the glacier to its terminus. The glacier watershed includes the steep slopes surrounding the glacier. These steep headwalls contribute snow and rock to the glacier surface through avalanches and rockfalls. We delineated stagnant ice near the terminus of the glacier based on the presence of hummocky topography and the lack of crevasses. All features, including glacier outlines, moraines, landslide deposits, scars, and fractures, were mapped at 1:20,000 scale.

In light of the high georeferencing errors, we did not directly compare the coordinates of the moraines and glacier fronts directly in the different datasets; rather we worked in relative coordinate systems. We defined reference lines between recognizable and relatively stable landscape features (moraines, tension cracks) and measured the distance (in meters) between these lines and the geomorphic features. Then, we compared the value of these distances in the different photo datasets. For Devastation Glacier, the reference line extends through the apex of the large 1947 landslide scar (Figure 4H). For Mosaic Glacier (Figure 5H), Job Glacier (Figure 6J), and Plinth Glacier (Figure 8I), the reference lines pass through gullies in their respective Little Ice Age moraines. In the case of Affliction Glacier, we established a line that intersects a tension crack near the glacier's Little Ice Age limit (Figure 7J). Distances from reference lines are not affected by georeferencing errors, as the models were not "optimized" on the GCP (see appendix A for processing details), but do include bundle adjustment errors, and polygon digitization errors, which depend on the mapping scale, operator precision, and the model precision (pixel error).This procedure provides relatively precise measurements even on poorly georeferenced maps, as long as the SfM bundle adjustment is precise enough. In this case, the PhotoScan bundle adjustment error (pixel error) of all datasets (0.6-2.2 m) is less than the graphical error (Gomarasca, 2009) at a scale of 1:20,000 (4 m), allowing this relative coordinate measurement approach. We calculated average glacier retreat rates by dividing distances between the glacier front and the reference line by the number of years between the datasets being compared. These rates are averages and do not consider non-linear fluctuations of the glacier terminus.

**Commentato [gr4]:** Added detailed processing in appendix to explain that by not "optimizing" the PhotoScan export we do not propagate the error of georef sources

# Geomorphic changes at Mount Meager volcano

**Commentato [gr5]:** I did not touch this

## Devastation

In 2016, Devastation Glacier was 3.7 km long and had an elevation range of 1400-2200 m asl. The glacier flows southeast from an ice cap that also feeds Mosaic and Affliction glaciers. The catchment area is 3 km$^2$ and has steep headwalls up to 0.7 km high (Table 3).

The landslides in 1947 and 1975 deposited debris on the glacier, which was subsequently deformed into arched debris ridges. The 1947 airphotos show landslide debris on the glacier (Figure 4A). The landslide scar has a triangular shape that is 0.26 km high and 0.27 km wide at the base. The landslide traveled 1.8 km, 1.7 km of which was on the glacier. The vertical drop was 0.5 km, thus the landslide had a *fahrböschung* (travel angle) of 15°. The landslide was constrained by lateral moraines and split into two lobes after overtopping a debris ridge on the glacier. Darker and lighter streaks are visible on the surface of the debris sheet. Active ice extends 1.2 km beyond the limit of the 1947 landslide deposit. The lowermost 0.5 km of the glacier appears to be stagnant. The glacier in 1947 was larger than at any other time in the 69-year photo period.

The glacier terminus retreated 1.7 km between 1947 and 2016. The average rate of retreat of the stagnant ice terminus was ~16 m yr$^{-1}$ between 1947 and 1973, ~76 m yr$^{-1}$ between 1973 and 1981, ~6 m yr$^{--1}$ between 1981 and 2006, and ~51 m yr$^{-1}$ between 2006 and 2016 (Figure 4I). The active ice terminus retreated at an average rate of ~14 m yr$^{-1}$ between 1947 and 1973 and ~88 m yr$^{-1}$ between 1973 and 1981. However, it advanced at an average rate of ~13 m yr$^{-1}$ between 1981 and 1990, before retreating ~10 m yr$^{-1}$ between 1990 and 2016 (Figure 4A-I).

By 1962 the glacier had deformed the 1947 landslide debris into two arched debris ridges. An arched ridge marked the up-glacier end of the debris sheet, and an S-shaped ridge was present at its lower limit (Figure 4B). Both ridges moved downstream at a rate of ~11 m yr$^{-1}$

between 1962 and 1981. In the 1981 photos, the two ridges are covered by debris of the large landslide that happened in 1975, but are still recognizable. Down glacier movement of the ridges increased to ~28 m $yr^{-1}$ between 1981 and 1990, but then decreased to ~6 m $yr^{-1}$ between 1990 and 2016. In the 2006 images, the lower ridge is unrecognizable and the upper ridge is eroded.

The slope that failed in 1975 is partly obscured by clouds and snow in the 1947, 1962, and 1973 photos, although antithetic scarps are visible on the lower part of the slope (Figure 4A, B, C). The 1981 photos clearly show the headscarp of the 1975 landslide, its travel path, and its debris on the glacier. The headscarp is 0.3 km wide and 1 km high (Figure 4D), and the deposit extends 6.7 km to the confluence of Devastation and Meager creeks. The vertical drop is about 1.2 km over that distance, yielding a *fahrböschung* of 10° (see Mokievsky-Zubok, 1977, for further details). By 1981, the landslide debris had been deformed into an arched debris ridge. This ridge advanced at an average rate of ~20 m $yr^{-1}$ between 1981 and 1990, ~9 m $yr^{-1}$ between 1990 and 2006, and ~5 m $yr^{-1}$ between 2006 and 2016. By 2006, the 1975 debris ridge had been breached (Figure 4F). The area between the breached 1975 debris ridge and the debris-free front of the glacier was a dissected flat surface.

### 1.1. Mosaic

In 2016 Mosaic Glacier had a length of 3 km and extended 3 km from 2200 to 1600 m asl. The north-facing basin in which the glacier sits has an area of 2.5 $km^2$. There are no significant cliffs that shed debris onto Mosaic Glacier.

Mosaic Glacier was obscured by clouds when the 1947 photos were taken. It retreated 1.9 km between 1951 and 2016 (Figure 5A-H). The average rate of retreat is ~49 m $yr^{-1}$ between 1951 and 1964,~20 m $yr^{-1}$ between 1964 and 2006, and ~45 m $yr^{-1}$ between 2006 and 2016 (Figure 5H). Sometime between 1962 and 1964, the western lateral moraine collapsed onto the glacier surface (Figure 5C). By 2006, this deposit has been eroded (Figure 5G).

### 1.2. Job

In 2016 Job Glacier was 2.8 km long, and descended from 2000 to 1200 m asl. The glacier is bordered by a steep headwall up to 0.5 km high. The large north-facing amphitheater (2.8 $km^2$) in which the glacier lies is partly the product of many Holocene landslides (Figure 1; Simpson et al., 2006; Friele et al., 2008).

The glacier in 1947 was larger than at any later time in the photographic record, and its snout was covered by debris. A streak of dark sediments is visible at the site where an ice cave and fumarole were discovered in 2016 (Roberti et al., 2016; Figure 6A)**.**The front of the glacier retreated 0.7 km between 1947 and 2016 (Figure 6A-K). The average rate of retreat is ~28 m $yr^{-1}$ between 1947 and 1964, and ~11 m $yr^{-1}$ between 1981 and 2016. The glacier advanced between 1964 and 1981 at an average rate of ~12 m $yr^{-1}$.

In 1990 photos, a debris streak 1 km long and up to 0.2 km wide is visible west of the glacier, indicating a recent landslide. The west and east valley flanks adjacent to the glacier show signs of instability (Roberti et al., 2018a).

### 1.3. Affliction

In 2016 Affliction Glacier was 3.2 km long and descended from 2200 m to 1500 m asl. It is bordered by a 0.3-km-high cliff that sheds debris onto the west part of the glacier. The glacier basin faces north and has an area of 3.6 $km^2$.

The glacier retreated 0.3 km from 1947 to 2016 (Figure 7A-K). The average rate of glacier retreat is ~15 m $yr^{-1}$ between 1947 and 1964, and ~6 m $yr^{-1}$ between 1981 and 2016. The glacier advanced at an average rate of ~11 m $yr^{-1}$ between 1964 and 1981. Both valley sides are marked by antithetic scarps and fractures.

### Plinth

Plinth Glacier is located in a steep-sided, northeast-facing amphitheatre (1.5 $km^2$) produced by the 2400-year-old eruption. In 2016 the glacier was 1.1 km long and extended from 1700 to 1200 m asl. The glacier is bordered by up to 1-km-high headwall (Table 3).

Clouds obscured the glacier in 1947. Between 1951 and 1990, it advanced at an average rate of ~8 m $yr^{-1}$. It receded between 1990 and 2006 at an average rate of ~15 m $yr^{-1}$, but advanced again between 2006 and 2016 at a rate of ~4m $yr^{-1}$ (Figure 8 A-H). In total the glacier has advanced slightly (0.07 km) since 1951.

## Discussion

### The value of historic photographs

We documented 69 years of glacier activity and landslides at Mount Meager by using SfM photogrammetric methods to process historic airphotos. This approach offers numerous opportunities to exploit an underutilized resource to quantify landscape change over the past 100 years. The method has not achieved its full potential in the past because of the difficulty of assessing the quality of the SfM-derived products derived from airphotos that are in poor condition or that lack adequate good ground control. Here we apply a method that does not require high-quality ground control and where measurements can be made in relative coordinate systems.

The advantages of processing historic airphotos with SfM include a fast, user-friendly workflow, retrieval of information from photos that cannot otherwise be processed due to lost metadata or poor photo condition, visualization of large areas at high resolution in 3D, and multiple years of coverage. This approach is also cheaper and faster than traditional digital photo interpretation: the cost of original digital data, when available, is 18.50$ per copy. The theoretical cost - theoretical because not all the images are available in digital format - of this study would have been 10,508 dollar. This cost may have been prohibitive for most scientific and professional geological assessment. In summary, we were able to document changes in the landscape that we could not otherwise have done, and boosted geohazard understanding at Mount Meager (e.g. Haley and Friele, 2018; Roberti et al., 2018a; Warwick et al., 2019). This approach could be more broadly applied to changes in Earth's surface caused, for example, by landslides, debris flows, fluvial processes, and land use, both for scientific research and for Geoscience professional practices, as shown by Cordilleran Geoscience (2018). New 3D datasets that can be generated using this approach may elucidate the effects of recent climate change and human impacts on landscapes. The datasets also have potential commercial and educational applications. Three-dimensional topographic models can now be easily visualized and analyzed in virtual and augmented reality environments (e.g. Onsel et al., 2018) and can be used to generate 3D time-lapse videos of surface changes (for example, see changes of Mosaic Glacier from 1951 to 2016 here).

**Commentato [gr6]:** check this

## Mount Meager's glaciers

We have provided a first-order description of the activity of Mount Meager glaciers over the past 69 years. Job, Affliction, and Plinth glaciers experienced minor advances in the late 1960s and 1970s, as did most glaciers in nearby Garibaldi Provincial Park (Koch et al., 2009). Devastation and Mosaic glaciers, however, retreated throughout the photo period (Figure 9).

### Devastation

**Commentato [gr7]:** I deleted some fo the moraine formation consideration

Debris on glaciers is commonly derived from rockfalls. If exhumed in the ablation zone, the debris provides an insulating cover to the ice (Anderson and Anderson, 2016). In contrast, the debris cover on Devastation Glacier appears to be mainly a product of large landslides directly onto the ablation zone. Devastation Glacier offers an opportunity to track the evolution of two rock avalanches from the time they emplaced debris on the glacier surface until the time the debris was deposited at the glacier front. When a landslide impacts the accumulation zone of a glacier, the debris decreases ablation until it is buried by snow. The debris moves down the glacier and is exposed in the ablation zone where it reduces surface melting. Commonly, the extensive debris-covered lower portion of the terminal zone of the glacier stagnates and slowly down-wastes. Eventually, the debris sheet is lowered onto ground without forming a frontal moraine. Based on this model, the 1947 and 1975 landslide debris move down the glacier at a decreasing velocity over time. Particularly instructive, is the acceleration of the 1947 debris ridge and a reduction in the rate of down-wasting of the stagnant ice lowermost portion of the glacier between 1981 and 1990, consistent with the role played by the 1975 landslide debris. The 1947 and 1975 landslide debris and the ridges, are progressively degraded and dispersed by the glacier flow, generating hummocky topography at the stagnant front of the glacier. The debris is then gradually removed by proglacial stream erosion.

Notably, Devastation Glacier was debris covered prior to the 1947 landslide, probably due to a large landslide onto the glacier in 1931 (Carter, 1932) and perhaps other landslides (e.g. number 4 in Figure 1). InSAR data indicate that the steep slopes bordering Devastation Glacier continue to deform, and more large landslides are expected in this basin in the future (Roberti et al., 2018a), further affecting the glacier activity. Any such landslides will further perturb the glacier and possibly override the climate drivers that determine the activity of glaciers that are not extensively debris-covered.

**Mosaic**

Rapid retreat of Mosaic Glacier between 1962 and 1964 may have caused the Little Ice Age lateral moraine to collapse onto the glacier, as documented by Blair (1994) in the Southern Alps of New Zealand. This landslide likely not affect the glacier’s mass balance because its deposit was limited to the glacier front. The debris did not form a moraine in the glacier foreland. The lack of significant debris cover on Mosaic Glacier may explains why it behaved differently than nearby Job and Affliction glaciers over the photo period.

**Job**

Like Mosaic and Affliction glaciers, Job Glacier experienced accelerated retreat between 1962 and 1964. The glacier advanced in the late 1960s and 1970s.

Diffuse volcanic gas emissions have been observed in the Job catchment the 1970s (Peter Read, personal communication 2018) and were studied during geothermal exploration in the area (Nevin Sadlier-Brown and Goodbrand, 1980, 1981). The presence of fumaroles near the center of a landslide collapse scar may indicate a relation between hydrothermal activity and large Holocene landslides in the basin (Figure 1; Friele et al., 2008). InSAR data show that other slopes in the catchment are unstable and slowly moving (Roberti et al., 2018a).The relation between past and ongoing deformation and hydrothermal activity needs to be addressed in more detail.

**Affliction**

Affliction Glacier, like Job Glacier, retreated at an accelerated rate between 1962 and 1964, and advanced in the late 1960s and 1970s. The debris-covered streak on the west side of the glacier, which is visible in each data set, is a product of frequent rockfalls from the cliff above. (Bovis 1990) documented slope deformation on the valley flank, and Roberti et al., (2018a) measured current displacement rate by InSAR.

**Plinth**

Plinth Glacier is the only glacier on the Mount Meager volcanic complex that was larger at the end of the photo period than at the beginning. It also is the smallest and lowest of the glaciers that we studied (Table 3). The high headwalls of the 2360 yr BP eruption that surround the glacier reduce incident short wave radiation and are likely the reason the glacier has advanced, albeit by only 0.07 km since 1951. In addition, the headwall funnel snow avalanches onto the glacier, supplementing mass added by winter snowfall. The headwalls consist of highly fractured and altered volcanic rocks, and generate numerous rockfall and small rock avalanches that introduce debris onto the glacier.

In cases where supraglacial debris is thick, it may completely suppress surface melting, causing the glacier to slowly advance downvalley, in a manner similar to a rock glacier (Menounos et al., 2013; Anderson and Anderson, 2016; Anderson et al., 2018). Plinth Glacier may be an example of this behavior, but in situ measurements and observations are needed to test this hypothesis. In a warming climate, thawing of formerly frozen rock walls above glacier surfaces may increase the incidence of rockfalls (Gruber and Haeberli, 2007; Pogliotti et al., 2008), leading to a thickening of debris on glaciers, especially if the rock walls comprise highly fractured and altered volcanic material. Terrestrial laser scanner and photogrammetry surveys could determine rockfall magnitude and frequency from the headwalls of Plinth Glacier, as has been done locally in the European Alps (Fischer et al., 2006; Bertotto et al., 2015).

## 1. Conclusions

We have applied Structure from Motion to historic vertical aerial photographs to document 69 years of glacier and landslide activity at Mount Meager, focusing on Devastation, Mosaic, Job, Affliction, and Plinth glaciers. We draw the following conclusion for this study:

- SfM is superior to classic photogrammetry for reconstructing geomorphic changes from historical aerial photographs, given in cases where ground control, and image and flight metadata are unavailable. We present a workflow that does not require high-precision ground control by making measurements in a relative coordinate system.
- 3D historic photographic reconstruction has many unrealized applications. It provides value to otherwise unused datasets and facilitates documentation of recent geomorphic changes. Visualization of 3D models derived from these photos also helps

non-scientific users understand natural processes and the effects of modern climate change on the landscape.

- Of the five glaciers studied, debris-free Mosaic Glacier retreated most over the photo period (1.9 km in 69 years). Devastation Glacier retreated 1.7 km, but was perturbed by large landslides in 1947 and 1975.
- The 1947 and 1975 landslides temporarily increased ice velocity on Devastation Glacier and led to the stagnation of the glacier front.
- Job and Affliction glaciers advanced in the late 1960s and 1970s, but only 0.7 and 0.3 km, respectively. Job Glacier is located in a large landslide-generated amphitheatre in which there has been fumarolic activity, probably since at least 1947. Plinth Glacier is located in the crater of the 2400-year-old Mount Meager eruption and is the only glacier that advanced over the entire study period.

## 2. Acknowledgments

We thank Peter Read for sharing his knowledge of Mount Meager volcano. Discussions with Davide Donati helped to formulate some SfM ideas. Financial support for the 2015 Lidar data acquisition was provided by NSERC through Discovery Grants to Clague and Menounos and the Canada Foundation for Innovation (Menounos). Natural Resources Canada (NRCan), through Melanie Kelman, provided funds for acquisition of the 2016 Lidar dataset. Financial support for Roberti's PhD project was provided by the "End of an Arc: The Remarkable Life and Death of a Volcanic Arc" project (a French-Canadian partnership), Simon Fraser University (SFU) Graduate and Teaching assistant fellowships, and Ward's SFU Departmental Chair funds.

## 3. References

Anderson, L.S., Anderson, R.S., 2016. Modeling debris-covered glaciers: Response to steady debris deposition. Cryosphere 10, 1105–1124. doi:10.5194/tc-10-1105-2016

Anderson, R.S., Anderson, L.S., Armstrong, W.H., Rossi, M.W., Crump, S.E., 2018. Glaciation of alpine valleys: The glacier – debris-covered glacier – rock glacier continuum. Geomorphology 311, 127–142. doi:10.1016/j.geomorph.2018.03.015

ASPRS, 2014. ASPRS Positional Accuracy Standards for Digital Geospatial Data. Photogramm. Eng. Remote Sens. 81, 1–26. doi:10.14358/PERS.81.3.A1-A26

Bakker, M., Lane, S.N., 2016. Archival photogrammetric analysis of river-floodplain systems using Structure from Motion (SfM) methods. Earth Surf. Process. Landforms. doi:10.1002/esp.4085

Bertotto, S., Perotti, L., Bacenetti, M., Damiano, E., Chiarle, M., Giardino, M., 2015. Integrated Geomatic Techniques for Assessing Morphodynamic Processes and Related Hazards in Glacial and Periglacial Areas (Western Italian Alps) in a Context of Climate Change, in: Lollino, G., Manconi, A., Clague, J., Shan, W., Chiarle, M. (Eds.), Engineering Geology for Society and Territory - Volume 1: Climate Change and Engineering Geology. pp. 1–572. doi:10.1007/978-3-319-09300-0

Bjørk, A.A., Kjær, K.H., Korsgaard, N.J., Khan, S.A., Kjeldsen, K.K., Andresen, C.S., Box, J.E., Larsen, N.K., Funder, S., 2012. An aerial view of 80 years of climate-related glacier fluctuations in southeast Greenland. Nat. Geosci. 5, 427–432. doi:10.1038/ngeo1481

Blair, R.W., 1994. Moraine and Valley Wall Collapse due to Rapid Deglaciation in Mount Cook National Park, New Zealand. Mt. Res. Dev. 14, 347–358. doi:10.2307/3673731

Bovis, M.J., 1990. Rock-slope deformation at Affliction Creek, southern Coast Mountains, British Columbia. Can. J. Earth Sci. 27, 243–254. doi:10.1139/e90-024

Bovis, M.J., Jakob, M., 2000. The July 29, 1998, debris flow and landslide dam at Capricorn Creek, Mount Meager Volcanic Complex, southern Coast Mountains, British Columbia. Can. J. Earth Sci. 37, 1321–1334. doi:10.1139/e00-042

Carrivick, J.L., Smith, M.W., Quincey, D.J., 2016. Structure from motion in geosciences.

Carter, M., 1932. Exploration in the Lillooet River Watershed. Can. Alp. J. 21, 19–28.

Cecchi, E., van Wyk de Vries, B., Lavest, J.M., Harris, A., Davies, M., 2003. N-view reconstruction: A new method for morphological modelling and deformation measurement in volcanology. J. Volcanol. Geotherm. Res. 123, 181–201.

doi:10.1016/S0377-0273(03)00035-0

Cecchi, E.M.C., Avest, J.E.A.N.A.R.C.L., An, B.E. V, Ries, W.Y.K.D.E. V, 2002. VIDEOGRAMMETRIC RECONSTRUCTION APPLIED TO VOLCANOLOGY : PERSPECTIVES FOR A NEW MEASUREMENT TECHNIQUE IN VOLCANO MONITORING 31–36.

Chandler, J., 1999. Effective application of automated digital photogrammetry for geomorphological research. Earth Surf. Process. Landforms 24, 51–63. doi:10.1002/(SICI)1096-9837(199901)24:1<51::AID-ESP948>3.0.CO;2-H

Cordilleran Geoscience, 2018. The Village of Lions Bay : A Natural Hazards Assessment Area Strategy for Coastal, Creek and Hillslope Hazards.

Fischer, L., Kääb,  a., Huggel, C., Noetzli, J., 2006. Geology, glacier retreat and permafrost degradation as controlling factors of slope instabilities in a high-mountain rock wall: the Monte Rosa east face. Nat. Hazards Earth Syst. Sci. 6, 761–772. doi:10.5194/nhess-6-761-2006

Fonstad, M.A., Dietrich, J.T., Courville, B.C., Jensen, J.L., Carbonneau, P.E., 2013. Topographic structure from motion: A new development in photogrammetric measurement. Earth Surf. Process. Landforms 38, 421–430. doi:10.1002/esp.3366

Friele, P.A., Jakob, M., Clague, J.J., 2008. Hazard and risk from large landslides from Mount Meager volcano, British Columbia, Canada. Georisk Assess. Manag. Risk Eng. Syst. Geohazards 2, 48–64. doi:10.1080/17499510801958711

Furukawa, Y., Ponce, J., 2010. Accurate , Dense , and Robust Multiview Stereopsis 32, 1362–1376.

Girardeau-Montaut, D., 2018. Cloud Compare.

Gomarasca, M.A., 2009. Basics of geomatics, Basics of Geomatics. Springer Netherlands.

Gomez, C., 2014. Digital photogrammetry and GIS-based analysis of the bio-geomorphological evolution of Sakurajima Volcano, diachronic analysis from 1947 to 2006. J. Volcanol. Geotherm. Res. 280, 1–13. doi:10.1016/j.jvolgeores.2014.04.015

Gomez, C., Hayakawa, Y., Obanawa, H., 2015. A study of Japanese landscapes using structure from motion derived DSMs and DEMs based on historical aerial photographs: New opportunities for vegetation monitoring and diachronic geomorphology.

Geomorphology 242, 11–20. doi:10.1016/j.geomorph.2015.02.021

Gruber, S., Haeberli, W., 2007. Permafrost in steep bedrock slopes and its temperatures-related destabilization following climate change. J. Geophys. Res. Earth Surf. 112, 1–10. doi:10.1029/2006JF000547

Haley, J., Friele, P., 2018. Landslide Risk Management for the Construction and Operation of the Upper Lillooet River Hydroelectric Facility near Pemberton , BC, in: Geohazards7 Engineering Resiliency in a Changing Climate. Canmore.

Hirschmüller, H., Buder, M., Ernst, I., 2012. Memory efficient semi-global matching. ISPRS Ann. Photogramm. Remote Sens. Spat. Inf. Sci. I–3, 371–376. doi:10.5194/isprsannals-I-3-371-2012

James, M.R., Robson, S., 2012. Straightforward reconstruction of 3D surfaces and topography with a camera : Accuracy and geoscience application 117, 1–17. doi:10.1029/2011JF002289

James, M.R., Robson, S., d'Oleire-Oltmanns, S., Niethammer, U., 2017. Optimising UAV topographic surveys processed with structure-from-motion: Ground control quality, quantity and bundle adjustment. Geomorphology 280, 51–66. doi:https://doi.org/10.1016/j.geomorph.2016.11.021

Koch, J., Menounos, B., Clague, J.J., 2009. Glacier change in Garibaldi Provincial Park, southern Coast Mountains, British Columbia, since the Little Ice Age. Glob. Planet. Change 66, 161–178. doi:10.1016/j.gloplacha.2008.11.006

Krimmel, R.M., 1999. Analysis of difference between direct and geodetic mass balance measurements at South Cascade Glacier, Washington. Geogr. Ann. Ser. A Phys. Geogr. 81, 653–658. doi:10.1111/j.0435-3676.1999.00093.x

Lane, S.N., James, T.D., Crowell, M.D., 2000. Application of digital photogrammetry to complex topography for geomorphological research. Photogramm. Rec. 16, 793–821. doi:10.1111/0031-868X.00152

Linder, W., 2009. Digital Photogrammetry: a practical course. Springer, Berlin.

Lowe, D.G., 1999. Object recognition from local scale-invariant features. Proc. Seventh IEEE Int. Conf. Comput. Vis. 2, 1150–1157. doi:10.1109/ICCV.1999.790410

Lucchesi, S., Giardino, M., Perotti, L., 2013. Applications of high-resolution images and

DTMs for detailed geomorphological analysis of mountain and plain areas of NW Italy. Eur. J. Remote Sens. 46, 216–233. doi:10.5721/EuJRS20134612

Menounos, B., Clague, J.J., Clarke, G.K.C., Marcott, S.A., Osborn, G., Clark, P.U., Tennant, C., Novak, A.M., 2013. Did rock avalanche deposits modulate the late Holocene advance of Tiedemann Glacier, southern Coast Mountains, British Columbia, Canada? Earth Planet. Sci. Lett. 384, 154–164. doi:10.1016/j.epsl.2013.10.008

Mertes, J.R., Gulley, J.D., Benn, D.I., Thompson, S.S., Nicholson, L.I., 2017. Using structure-from-motion to create glacier DEMs and orthoimagery from historical terrestrial and oblique aerial imagery. Earth Surf. Process. Landforms. doi:10.1002/esp.4188

Micheletti, N., Chandler, J.H., Lane, S.N., 2015. Structure from motion ( SFM ) photogrammetry, in: Cook, S., Clarke, L., Nield, J. (Eds.), Geomorphological Techniques. British Society for Geomorphology, London, pp. 1–12.

Mokievsky-Zubok, O., 1977. Glacier-caused slide near Pylon Peak, British Columbia. Can. J. Earth Sci. 15, 1039–1052.

Mölg, N., Bolch, T., 2017. Structure-from-Motion Using Historical Aerial Images to Analyse Changes in Glacier Surface Elevation. Remote Sens. 9, 1021. doi:10.3390/rs9101021

Natural Resources Canada, 2013. Canadian Digital Elevation Model Product Specifications Edition 1.1. Gov. Canada, Nat. Resour. Canada, Map Inf. Branch, GeoGratis Client Serv. 2638, 11.

NSBG (Nevin Sadlier-Brown Goodbrand Ltd), 1981. Report gt20 for B.C. Hydro and Power Authority. Meager Mountain Geothermal Project Status of Environmental Studies Baseline Data Collection Program 1980.

NSBG (Nevin Sadlier-Brown Goodbrand Ltd), 1980. Report gt14 for B.C Hydro and Power Authority. Meager Mountain Geothermal Project Status of Environmental Studies Baseline data Collection Program 1980.

Onsel, I.E., Donati, D., Stead, D., Chang, O., 2018. Applications of virtual and mixed reality in rock engineering, in: ARMA 52nd US Rock Mechanics/Geomechanics Symposium. 17-20 June 2018, Seattle.

Pogliotti, P., Cremonese, E., Morra di Cella, U., Gruber, S., Giardino, M., 2008. Thermal diffusivity variability in alpine permafrost rock walls. 9th Int. Conf. Permafrost, Fairbanks, Alaska, 29 June 2008 - 03 July 2008 1427–1432. doi:10.5167/uzh-3098

Remondino, F., Spera, M.G., Nocerino, E., Menna, F., Nex, F., 2014. State of the art in high density image matching. Photogramm. Rec. 29, 144–166. doi:10.1111/phor.12063

Roberti, G., Ward, B., van Wyk de Vries, B., Falorni, G., Menounos, B., Friele, P., Williams-Jones, G., Clague, J.J., Perotti, L., Giardino, M., Baldeon, G., Freschi, S., 2018a. Landslides and glacier retreat at Mt. Meager volcano: Hazard and risk challenges, in: Geohazards7 Engineering Resiliency in a Changing Climate. June 3 - 6, 2018 Canmore, AB.

Roberti, G., Ward, B., van Wyk de Vries, B., Friele, P., Perotti, L., Clague, J.J., Giardino, M., 2018b. Precursory slope distress prior to the 2010 Mount Meager landslide, British Columbia. Landslides 15, 637–647. doi:10.1007/s10346-017-0901-0

Roberti, G., Ward, B., van Wyk de Vries, B., Friele, P.A., Perotti, L., Clague, J.J., Giardino, M., 2017. Precursor slope distress leading up to the 2010 Mount Meager landslide, British Columbia. EGU 19, 2017.

Roberti, G., Ward, B.C., van Wyk de Vries, B., Williams-Jones, G., Falorni, G., Iannacone, J.P., Giardino, M., Clague, J.J., Friele, P.A., 2016. Sector collapse and fumarole activity detected at Mt Meager, Canada, in: ILP Topo-Europe 2016 from Deep Earth to Surface: Integrating Lithosphere Dynamics with Rift Basins and Margins: A Joint Meeting of the TOPO-EUROPE Programme and ILP Task Forces Sedimentary Basins (VI), Subducted Lithosphere (IV), Magma and Lithosphere (II. Clermont Ferrand, 5-6 October 2016.

Simpson, K.A., Stasiuk, M., Shimamura, K., Clague, J.J., Friele, P., 2006. Evidence for catastrophic volcanic debris flows in Pemberton Valley, British Columbia. Can. J. Earth Sci. 43, 679–689. doi:10.1139/e06-026

Snavely, N., Seitz, S.M., Szeliski, R., 2008. Modeling the world from Internet photo collections. Int. J. Comput. Vis. 80, 189–210. doi:10.1007/s11263-007-0107-3

Spreafico, M.C., Perotti, L., Cervi, F., Bacenetti, M., Bitelli, G., Girelli, V.A., Mandanici, E., Tini, M.A., Borgatti, L., 2015. Terrestrial Remote Sensing techniques to complement conventional geomechanical surveys for the assessment of landslide hazard: The San Leo case study (Italy). Eur. J. Remote Sens. 48, 639–660. doi:10.5721/EuJRS20154835

Szeliski, R., 2010. Computer Vision : Algorithms and Applications. Computer (Long. Beach. Calif). 5, 832. doi:10.1007/978-1-84882-935-0

Tennant, C., Menounos, B., 2013. Glacier change of the Columbia Icefield, Canadian Rocky Mountains, 1919-2009. J. Glaciol. 59, 671–686. doi:10.3189/2013JoG12J135

Ullman, S., 1979. The interpretation of structure from motion. Proc. R. Soc. Lond. B. Biol. Sci. 203, 405–426. doi:10.1098/rspb.1979.0006

Warwick, R.K., Williams-Jones, G., Witter, J., 2019. Comprehensive Volcanic-Hazard Map for Mount Meager Volcano , Southwestern British Columbia ( Part of NTS 092J ) Comprehensive Volcanic-Hazard Map for Mount Meager Volcano , Southwestern British Columbia ( Part of NTS 092J ). doi:10.13140/RG.2.2.30919.75688

## Table captions

**Table 1** **Airphotos and PhotoScan model characteristics.**

**Table 2** **$RMSE_x$, $RMSE_y$, $RMSE_z$, $RMSE_r$, HA 95, and VA 95 for the different photo datasets.**

**Table 1** **Glacier parameters. N = north; NE = Northeast; SE = southeast. a = referred to the 1947 dataset. b = referred to the 1951 dataset.**

## List of figures

**Commentato [gr8]:** added Figure 2 and 3

**Figure 1** **Overview of the Mount Meager volcanic complex showing the extent of glaciers in 2016, landslide scars and their reference studies, unstable areas, and figure locations. Insets: A) Figure 4; B) Figure 5; C) Figure 6; D) Figure 7; E) Figure 8.**

**Figure 2** **SfM workflow from photo digitization to orthophoto, DEM export, and quality control**

**Figure 3** **A) Shaded relief model of the 1990 and 2006 photo dataset and the DEM of difference over the pre-2010 landslide failure area. B) Shaded relief model of the 1951 and 1990 and the DEM of difference over Devastation Valley. Glacier frontal retreat, some glacier thickening and 1998 and 1975 landslide scar, are visible in the DEM of difference. The elevation difference in stable areas is 10.6 m. Note the artifacts in the 1951 sheded relief.**

**Figure 4** **Devastation Valley, 1947-2016, showing changes in Devastation Glacier, moraines, landslide deposits, landslide scars, and cracks. A) 1947: glacier at its maximum extent; note the 1947 landslide deposit. B) 1962: active ice upstream of the 1947 landslide deposit has deformed the landslide debris into a flow-transverse arched ridge. C) 1973: the front of the debris-covered glacier has receded, and the 1947 landslide debris has moved farther downvalley. D) 1981: active ice upstream of the 1975 landslide has deformed the debris into a flow-transverse arched ridge, and the glacier front has receded farther; note the 1975 landslide scar. E) 1990: active ice upstream of the 1975 landslide has deformed the debris into a flow-transverse arched ridge; the stagnant glacier front has receded farther; F) 2006: further retreat of the glacier. G) 2016 (Lidar data): further retreat of the glacier. H) 2016 (Lidar data) showing glacier outline. I) Summary of changes in the position of the glacier front over the photo period. Note the decrease in the recession rate during the 1962-1973 and 1981-2006 periods. m = metres; yr =years.**

**Figure 5** **Mosaic valley, 1951-2016, showing changes in Mosaic Glacier, landslide deposits, landslide scars, and cracks. The glacier has retreated since 1951. A) 1951. B) 1962. C) 1964: note that part of the lateral moraine collapsed onto the glacier. D) 1973. E) 1981.F) 1990. G) 2006; note that the landslide deposit has been removed by erosion. H) 2016 (Lidar data). I) 2016 (Lidar data) showing glacier outline. J) Summary of changes in the position of the glacier front over the photo period. m = metres; yr = years.**

**Figure 6** **Job valley, 1947-2016, showing changes in Job Glacier, unstable slopes, landslide scars, landslide deposits, and fumaroles. The glacier retreated between 1947 and 1964, advanced between 1964 and 1981, and then retreated again between 1981 and 2016. A) 1947; note the dark spot on the glacier marking the location of a fumarole. B) 1951. C) 1962. D) 1964. E) 1973. F) 1981. G) 1990; note debris on the glacier. H) 2006. I) 2016 (Lidar data). J) 2016 (Lidar data), showing glacier outlines. K) Summary of changes in the position of the glacier front over the photo period.m = metres; yr =years.**

**Figure 7** **Affliction valley, 1947-2016, showing changes in Affliction Glacier and unstable slopes. Note persistent debris cover on the west side of the glacier. The glacier retreated between 1947 and 1964, advanced between 1964 and 1981, and then retreated again between 1981 and 2016. A) 1947. B) 1951. C) 1962. D) 1964. E) 1973. F) 1981. G) 1990. H) 2006. I) 2016 (Lidar data). J) 2016 (Lidar data), showing glacier outlines. K) Summary of changes in glacier front position during the photo period. m = metres; yr =years.**

**Figure 8** **Plinth Glacier, 1951-2016, showing glacier outlines and 2360-yr eruption crater/landslide scar. The glacier advanced between 1951 and 1990, retreated between 1990 and 2006, and advanced between 2006 and 2016. A) 1951. B) 1962. C) 1964. D) 1973. E) 1981. F) 1990. G) 2006. H) 2016 (Lidar data). I) 2016 (Lidar data) showing glacier outlines. J) Summary of changes in the glacier front position during the photo period. m = metres; yr =years.**

**Figure 9** **Comparison of average rates of glacier retreat/advance on Mount Meager between 1947 and 2016. '0' corresponds to the glacier front position in 2016.**

## Appendix A

**Commentato [gr9]:** Details on SfM processing

**Masking**. We masked out photo frames and inscriptions to speed up the processing and avoid the presence of artifacts in 3D models, orthophotos and DEMs. Two masking approaches were followed. For the color datasets (2006) we automatically selected the dark pixels of the photo frame and manually excluded annotations. For grayscale datasets (1947, 1951, 1962, 1964-65, 1973, and 1990), we manually masked the photo frames and inscription. The automatic was not suitable for the grayscale datasets as large areas in the images have the same dark tones as the frame

**Alignment**. To generate a point cloud, the software matches features between the photos, defines and filters key points, estimates the camera position and camera parameters (focal length, principal point location, and up to four radial and four tangential distortion coefficients) and reconstructs the scene structure. "High accuracy setting has been used for photo alignment, and image pair preselection was set to —Generic (in a first step image pairs are selected by matching photos using lower accuracy setting and then re-matched at higher accuracy).

The 2006, 1981, 1973, 1962, and 1947 photo datasets were aligned at "high" resolution, 1964 at "medium" resolution and 1990 at "lowest" resolution. The quality of the alignment refers to the size of the photo: at "high" setting the photos are matched at full resolution, while pictures are downscaled of a factor of four at every lower quality setting. We noticed that at "high" setting (full photo resolution) the software was over representing some zones of the photos generating clouds with a heterogeneous distribution of points. In those cases, decreasing of alignment quality led to point clouds with better distributed matches. After the point cloud generation we cleaned the models, deleting incorrectly projected points with manual and automatic selection methods.

Lower alignment quality generates less detailed models (and coarser final DEMs) but also less artifacts from trees, crevasses and zones of poor texture over ice and snowfields. Downscaling alignment quality means larger matching areas where small shadows and imperfections in the photos are not visible and considered during the matching. Only the larger features will be visible and contribute to the alignment.

For the1964 and 1990 datasets PhotoScan was not able to align all the pictures in one set. We had to align the different photo strips in separate chunks and later merge the models in one single point cloud matching by manually placed markers, and then proceeded with the next steps of the process.

**Referencing**. At this step ground control points (GCP) are identified to georeference the models. During georeferencing, a rigid seven parameter transformation is applied to translate, scale, and rotate the model to fit the, real world, scene location. Ideally, GCPs should be located in flat, stable areas, far from cliffs, easy to recognize, and of easy access. At Mount Meager, it is very challenging to find points with these characteristics. Snow and glaciers cover the volcano, the valley flanks have very active channels or are forested, and the access to the area is challenging and dangerous.

**Optimization**. The rigid transformation applied during georeferencing cannot correct non-linear error that may be present in the model. Non-linear errors can be related to poor picture overlap, object texture or shape, or lens and scanner deformation. In order to partially correct these types of error, PhotoScan recommends to —optimize the estimated point cloud, camera position, and camera parameters based on GCP position. However, if the GCPs have low accuracy, they can introduce extra errors. In our case, the GPS planimetric accuracy is larger than 10 m and the vertical accuracy is larger than 40 m, we estimated that the PhotoScan alignment precision was greater than the GCP accuracy and we did not proceed to the optimization of the point clouds. We optimized only the point clouds (1962,

1990) that showed an artificial exaggeration along the Z direction. In those cases, the optimization partially corrected the vertical exaggeration of the models.

**Dense Point Cloud**. PhotoScan increases the number of points generating a dense point cloud. It calculates the depth map for each photo and produces a large number of points, many of which can be outliers. It is advisable to use a ―depth filte to reduce the number of these points. We used the method ―aggressive‖ recommended for aerial photography. In areas of poor texture especially glaciers and snowfields) many incorrect points have been generated; those areas have an artificially rough aspect.

**Mesh**. PhotoScan interpolates polygons between the points to generate a 3D mesh surface. The setting ―Height field‖ where the interpolation direction is along Z axes is recommended for planar scenes and aerial photography. We used the suggested ―high value for the polygon count.

**Texture**. A texture of the 3D models is reconstructed here. We used the ―orthophoto‖ mode, where the texture is reconstructed with an orthographic projection. It works well with flat surfaces but not as well with vertical parts. The blending mode was set to ―mosaic‖ as recommended for aerial photography.

**Digital elevation model (DEM).** A rasterized version of the 3D model is generated at this step. Sparse, dense point clouds or mesh can be used as base for the DEM generation. We used the dense point cloud as source of the DEM.

**Orthomosaic**. The orthomosaic is generated on the DEM surface. The blending mode has been left to the default ―mosaic setting.

Table 1

| Year | Number of pictures | Approximate photo scale | Pixel size (m/pixel) | 3D error (pixel) | 3D model precision (m) | DEM pixel size (m/pixel) |
|---|---|---|---|---|---|---|
| 2006 | 114 | 1:13000 | 0.5 | 1.2 | 0.6 | 2 |
| 1990 | 89 | 1:13000 | 0.5 | 3.0 | 1.5 | 2.2 |
| 1981 | 51 | 1:20000 | 0.7 | 1.1 | 0.8 | 2.7 |
| 1973 | 116 | 1:13000 | 0.5 | 1.1 | 0.6 | 1.9 |
| 1964 | 29 | 1:25000 | 1.3 | 1.4 | 1.8 | 5 |
| 1962 | 108 | 1:15000 | 0.5 | 1.4 | 0.7 | 1.8 |
| 1951 | 11 | 1:60000 | 2.2 | 1 | 2.2 | 4.3 |
| 1947 | 50 | 1:20000 | 1.1 | 1.4 | 1.5 | 4.3 |

Table 2

| Year | RMSEx | RMSEy | RMSEr | RMSEz | HA 95 (m) | VA 95 (m) |
|---|---|---|---|---|---|---|
| 2006 | 10 | 9 | 13 | 25 | 23 | 49 |
| 1990 | 6 | 9 | 11 | 8 | 19 | 15 |
| 1981 | 11 | 12 | 16 | 40 | 28 | 78 |
| 1973 | 29 | 41 | 50 | 25 | 86 | 49 |
| 1964 | 23 | 28 | 36 | 30 | 62 | 59 |
| 1962 | 15 | 8 | 17 | 90 | 30 | 176 |
| 1951 | 13 | 22 | 25 | 14 | 25 | 28 |
| 1947 | 20 | 28 | 35 | 17 | 61 | 34 |

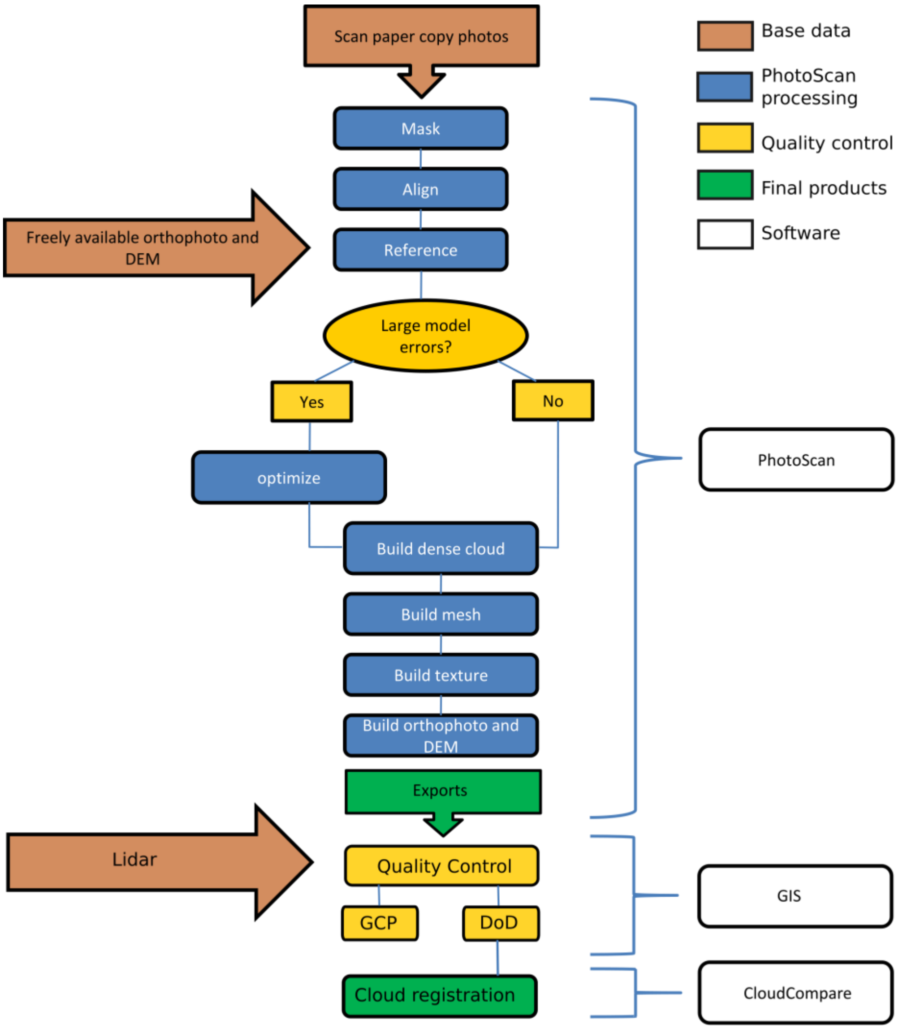

Scan paper copy photos
Mask
Align
Freely available orthophoto and DEM
Reference
Large model errors?
Yes
No
optimize
Build dense cloud
Build mesh
Build texture
Build orthophoto and DEM
Exports
Lidar
Quality Control
GCP
DoD
Cloud registration
Base data
PhotoScan processing
Quality control
Final products
Software
PhotoScan
GIS
CloudCompare


Figure 1

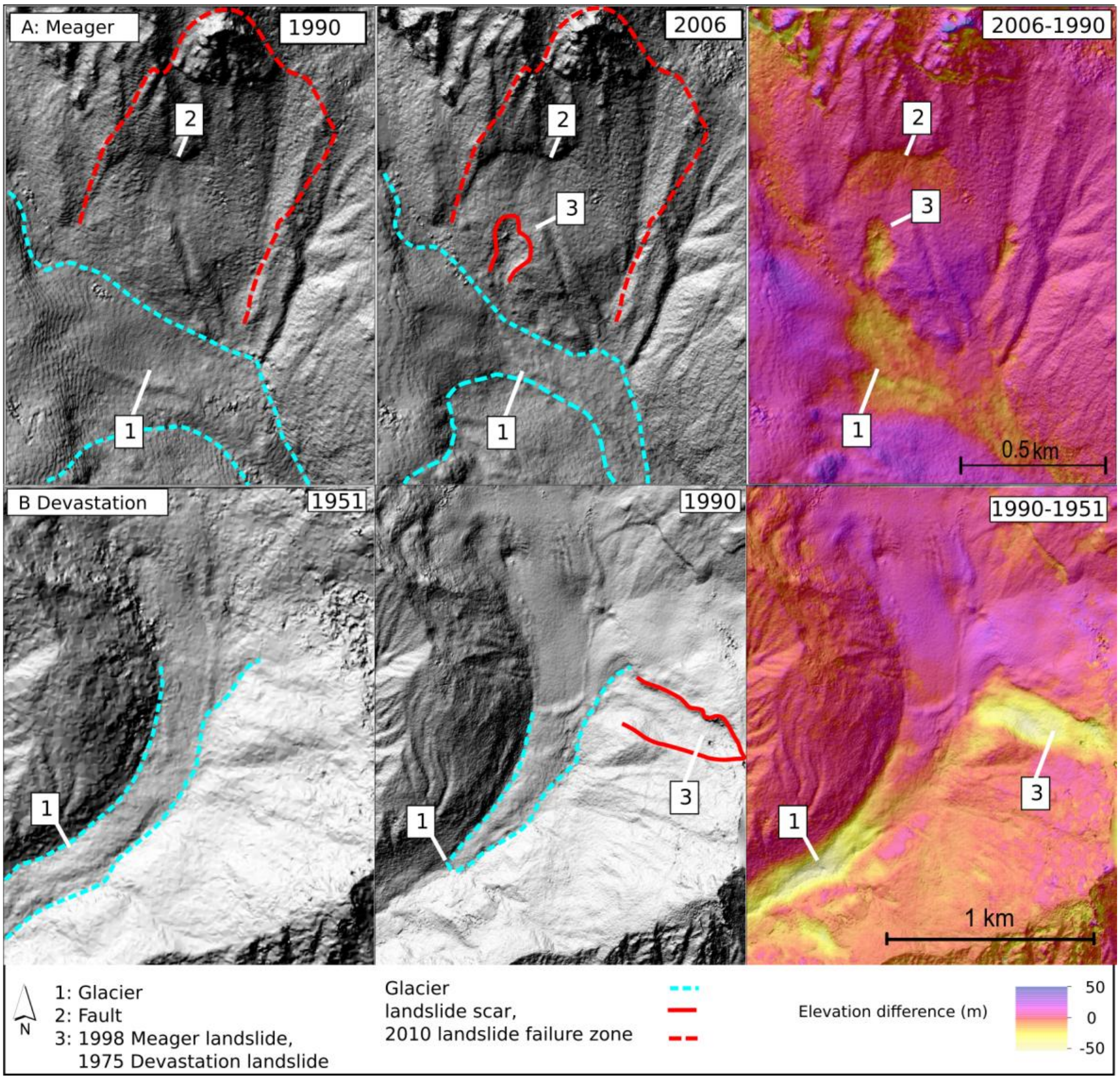
A: Meager
1990
2006
2006-1990
2
3
1
0.5 km
B Devastation
1951
1990
1990-1951
1 km
1: Glacier
2: Fault
3: 1998 Meager landslide, 1975 Devastation landslide
N
Glacier
landslide scar,
2010 landslide failure zone
Elevation difference (m)
50
0
-50

**Figure 2**

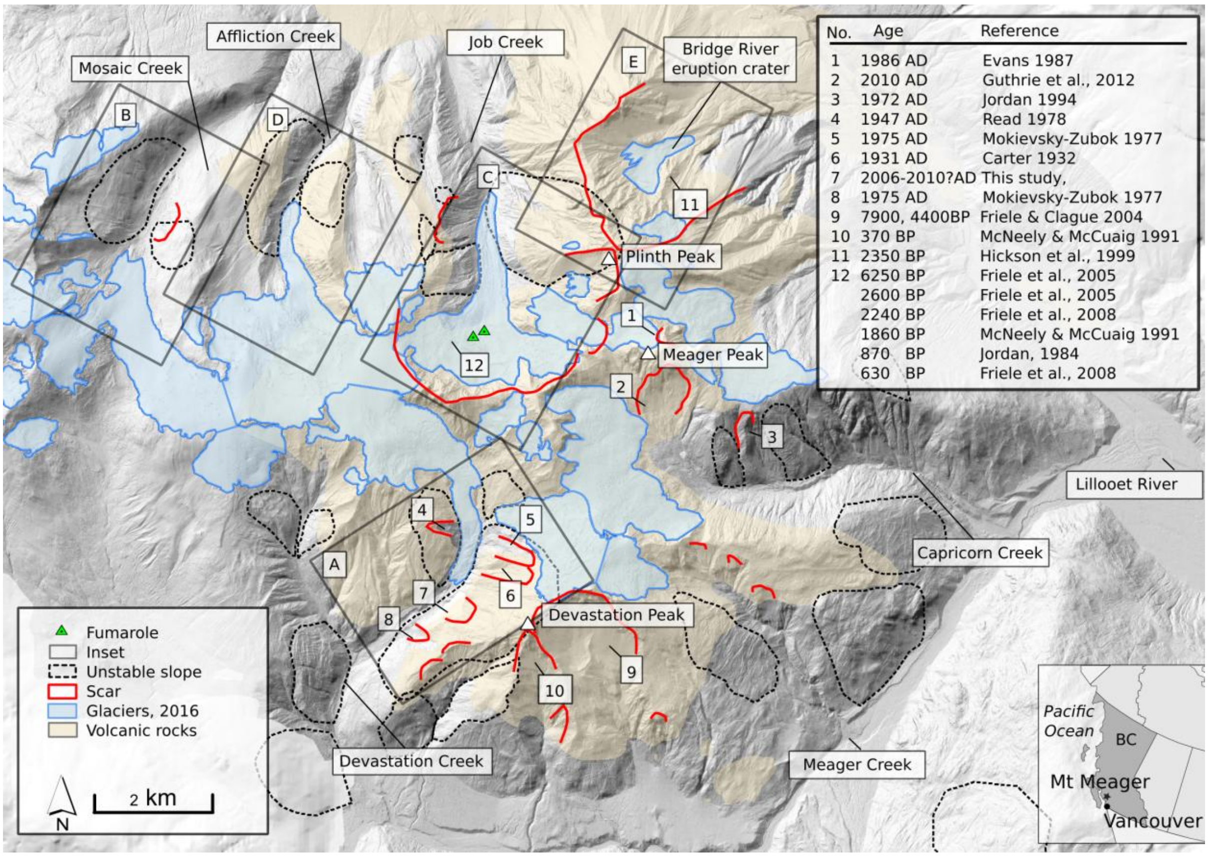

Mosaic Creek
Affliction Creek
Job Creek
Bridge River eruption crater
No. Age Reference
1 1986 AD Evans 1987
2 2010 AD Guthrie et al., 2012
3 1972 AD Jordan 1994
4 1947 AD Read 1978
5 1975 AD Mokievsky-Zubok 1977
6 1931 AD Carter 1932
7 2006-2010?AD This study,
8 1975 AD Mokievsky-Zubok 1977
9 7900, 4400BP Friele & Clague 2004
10 370 BP McNeely & McCuaig 1991
11 2350 BP Hickson et al., 1999
12 6250 BP Friele et al., 2005
2600 BP Friele et al., 2005
2240 BP Friele et al., 2008
1860 BP McNeely & McCuaig 1991
870 BP Jordan, 1984
630 BP Friele et al., 2008
Plinth Peak
Meager Peak
Lillooet River
Capricorn Creek
Devastation Peak
Devastation Creek
Meager Creek
Fumarole
Inset
Unstable slope
Scar
Glaciers, 2016
Volcanic rocks
2 km
N
Pacific Ocean
BC
Mt Meager
Vancouver


**Figure 3**

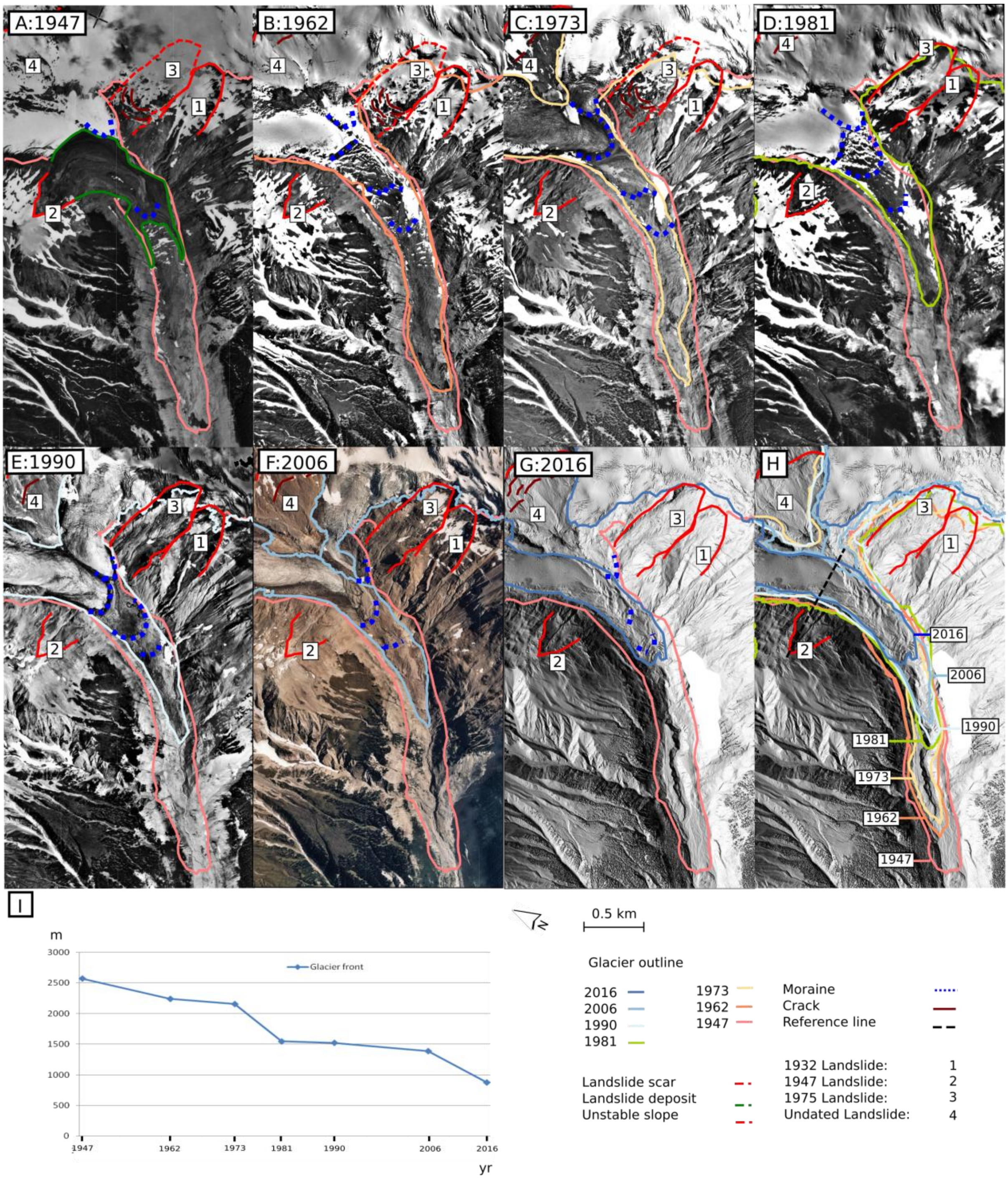
A:1947
B:1962
C:1973
D:1981
E:1990
F:2006
G:2016
H
I
m
Glacier front
yr
0.5 km
Glacier outline
2016
2006
1990
1981
1973
1962
1947
Moraine
Crack
Reference line
Landslide scar
Landslide deposit
Unstable slope
1932 Landslide: 1
1947 Landslide: 2
1975 Landslide: 3
Undated Landslide: 4

**Figure 4**

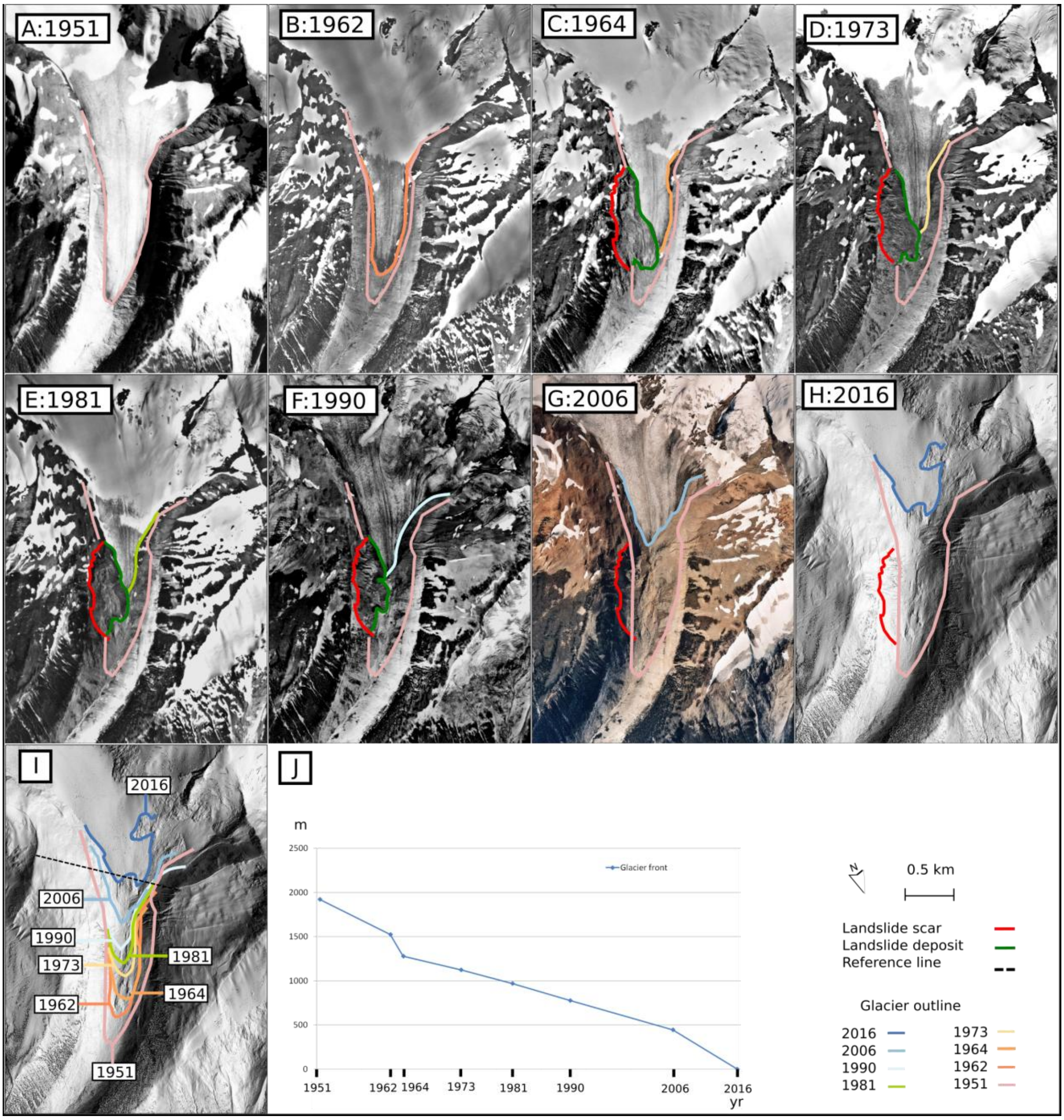
A:1951
B:1962
C:1964
D:1973
E:1981
F:1990
G:2006
H:2016
I
2016
2006
1990
1973
1962
1951
1981
1964
J
m
2500
2000
1500
1000
500
0
Glacier front
1951
1962
1964
1973
1981
1990
2006
2016
yr
N
0.5 km
Landslide scar
Landslide deposit
Reference line
Glacier outline
2016
2006
1990
1981
1973
1964
1962
1951

**Figure 5**

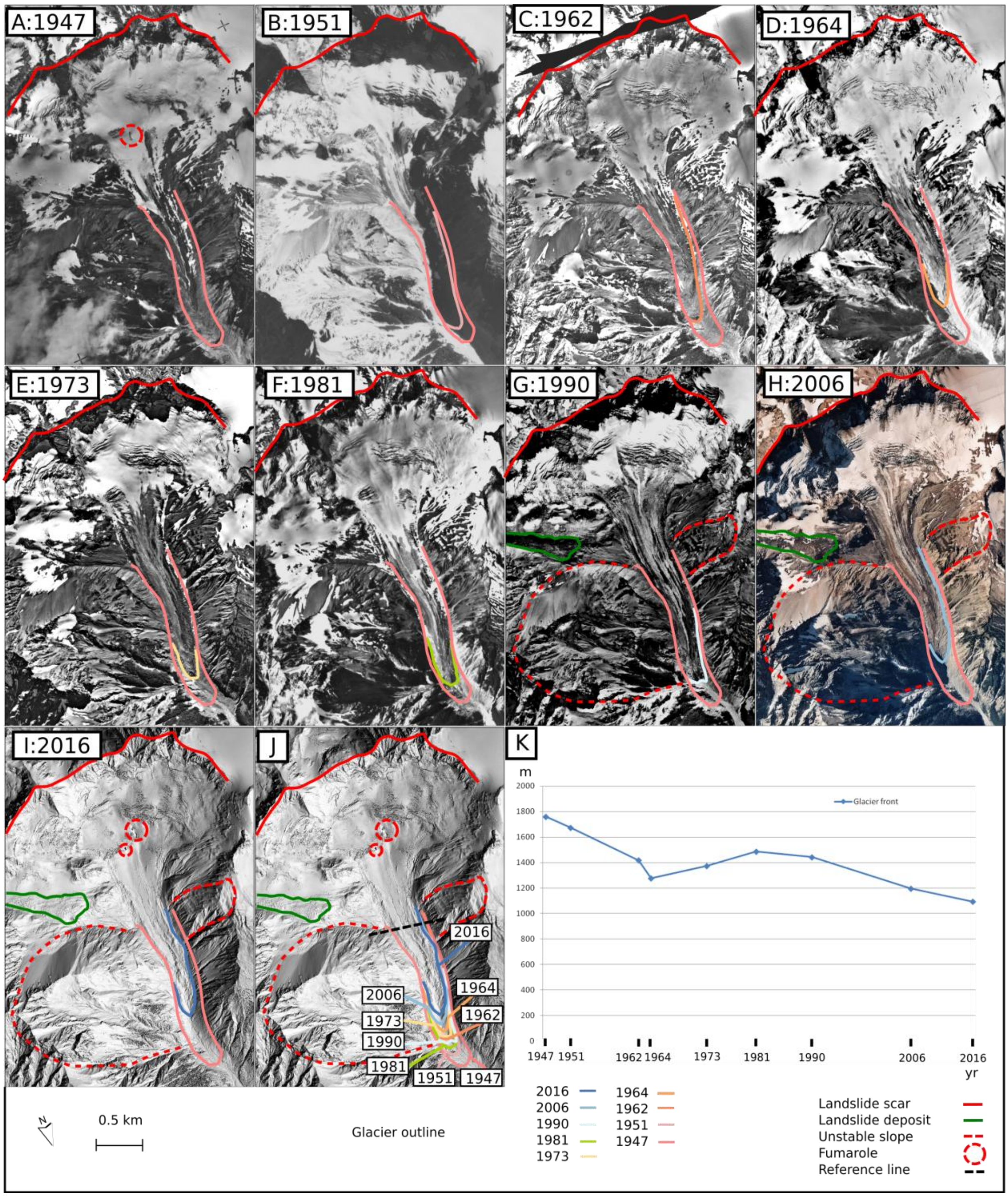

A:1947
B:1951
C:1962
D:1964
E:1973
F:1981
G:1990
H:2006
I:2016
J
2016
2006
1964
1973
1962
1990
1981
1951
1947
K
m
Glacier front
2000
1800
1600
1400
1200
1000
800
600
400
200
0
1947 1951 1962 1964 1973 1981 1990 2006 2016
yr
N
0.5 km
Glacier outline
2016
2006
1990
1981
1973
1964
1962
1951
1947
Landslide scar
Landslide deposit
Unstable slope
Fumarole
Reference line


Figure 6

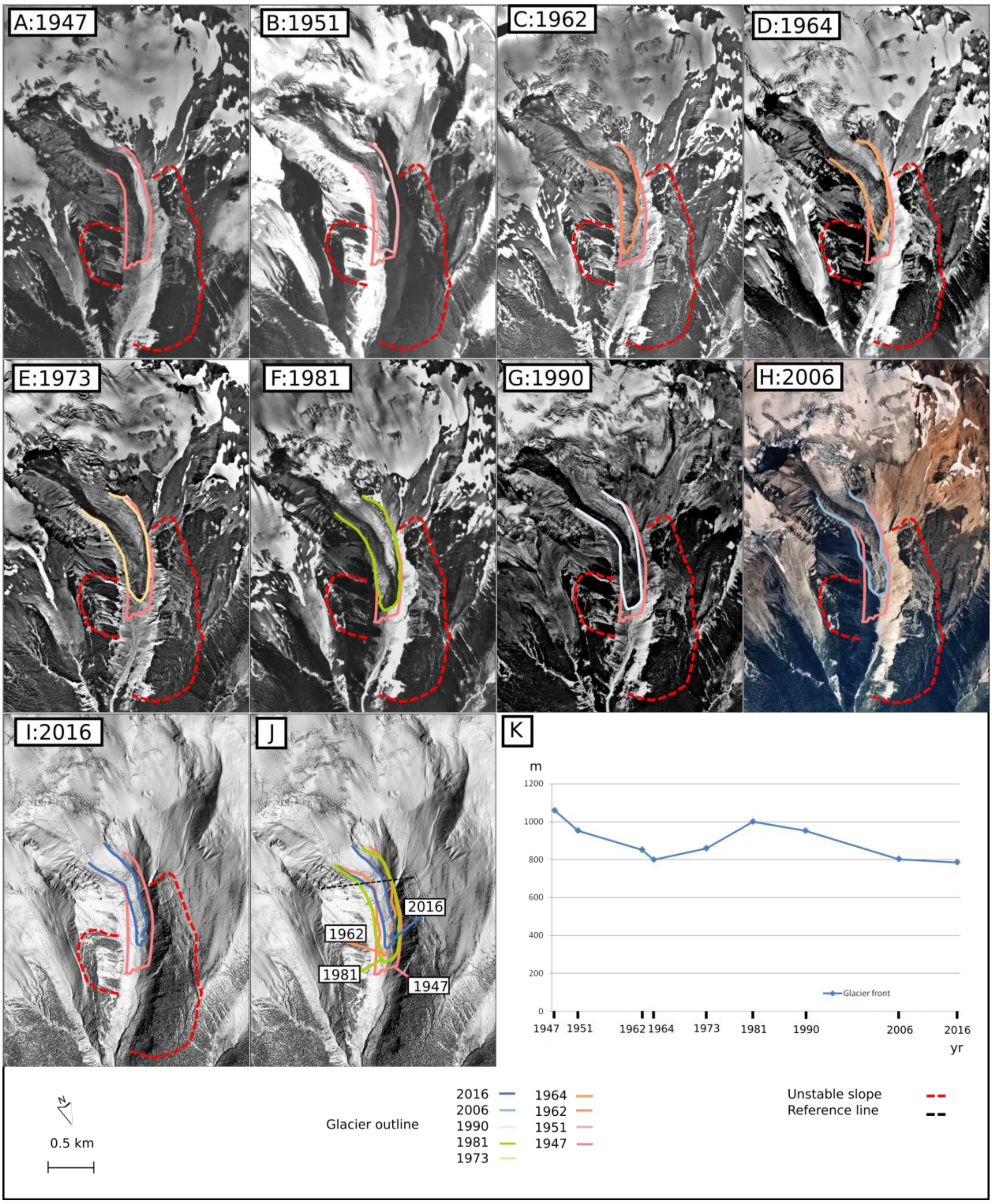

A:1947
B:1951
C:1962
D:1964
E:1973
F:1981
G:1990
H:2006
I:2016
J
2016
1962
1981
1947
K
m
1200
1000
800
600
400
200
0
Glacier front
1947
1951
1962
1964
1973
1981
1990
2006
2016
yr
N
0.5 km
Glacier outline
2016
2006
1990
1981
1973
1964
1962
1951
1947
Unstable slope
Reference line


Figure 7

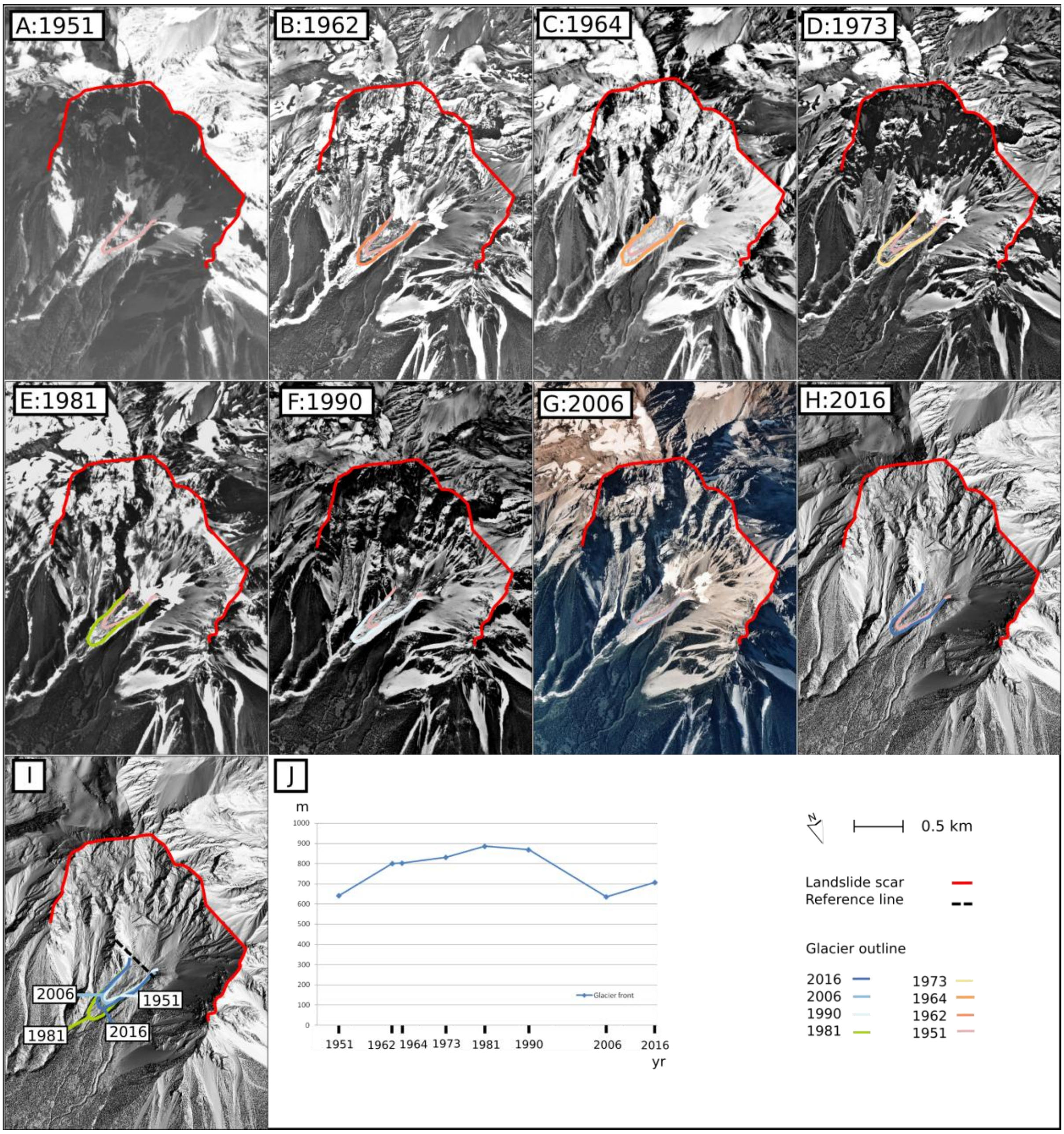

A:1951
B:1962
C:1964
D:1973
E:1981
F:1990
G:2006
H:2016
I
2006
1951
1981
2016
J
m
1000
900
800
700
600
500
400
300
200
100
0
Glacier front
1951
1962
1964
1973
1981
1990
2006
2016
yr
N
0.5 km
Landslide scar
Reference line
Glacier outline
2016
2006
1990
1981
1973
1964
1962
1951


Figure 8

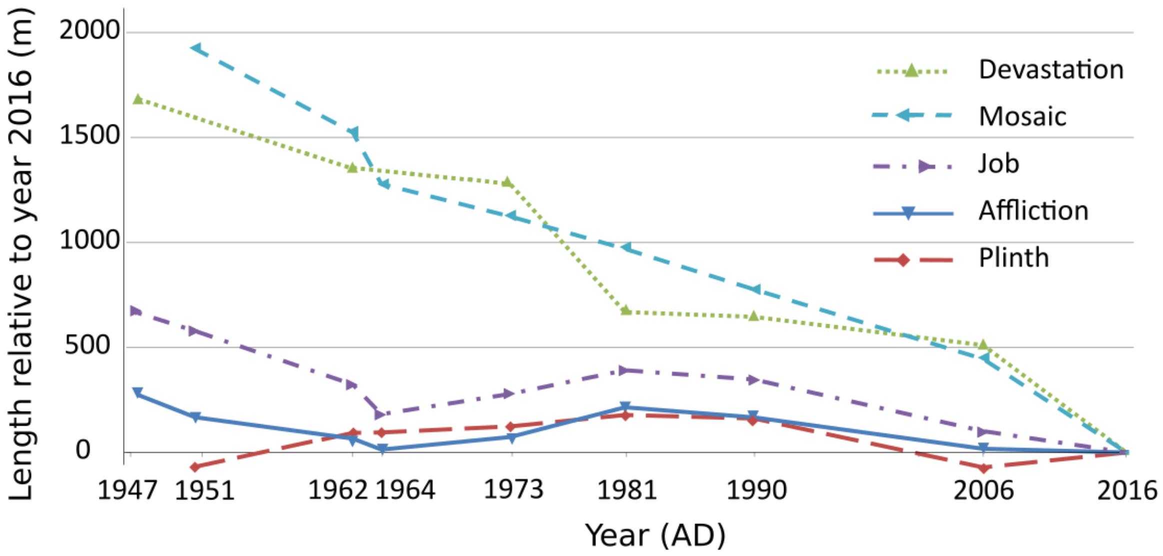


Figure 9

Table 3

| Glacier | Accumulation zone elevation (m. asl) | Glacier front elevation in 2016 (m. asl) | Glacier front elevation in 1947/51 (m. asl) | Glacier length (km) | Head wall height (km) | Watershed ($km^2$) | Relative front position in 2016 (km) | Aspect |
|---|---|---|---|---|---|---|---|---|
| Devastation | 2200 | 1400 | 1150[a] | 3.7 | 0.7 | 3 | -1.7 | SE |
| Mosaic | 2200 | 1600 | 1500[b] | 3 | 0 | 2.5 | -1.9 | N |
| Job | 2000 | 1200 | 1100[a] | 2.8 | 0.5 | 4 | - 0.7 | N |
| Affliction | 2200 | 1500 | 1350[a] | 3.2 | 0.3 | 3.6 | - 0.3 | N |
| Plinth | 1700 | 1200 | 1250[b] | 1.1 | 1 | 1.5 | + 0.07 | NE |